Environmental Science & Technology

Article

pubs.acs.org/est

Pore-Scale Controls on Calcite Dissolution Rates from Flow-through Laboratory and Numerical Experiments

Sergi Molins,*[,†] David Trebotich,[‡] Li Yang,[†] Jonathan B. Ajo-Franklin,[†] Terry J. Ligocki,[‡] Chaopeng Shen,[‡] and Carl I. Steefel[†]

[†]Earth Sciences Division and [‡]Computational Research Division, Lawrence Berkeley National Laboratory, One Cyclotron Road, Berkeley, California 94720, United States

Supporting Information

ABSTRACT: A combination of experimental, imaging, and modeling techniques were applied to investigate the pore-scale transport and surface reaction controls on calcite dissolution under elevated pCO_2 conditions. The laboratory experiment consisted of the injection of a solution at 4 bar pCO_2 into a capillary tube packed with crushed calcite. A high resolution pore-scale numerical model was used to simulate the experiment based on a computational domain consisting of reactive calcite, pore space, and the capillary wall constructed from volumetric X-ray microtomography images. Simulated pore-scale effluent concentrations were higher than those measured by a factor of 1.8, with the largest component of the discrepancy related to uncertainties in the reaction rate model and its parameters. However, part of the discrepancy was apparently due to mass transport limitations to reactive surfaces, which were most pronounced near the inlet where larger diffusive boundary layers formed around grains and in slow-flowing pore spaces that exchanged mass by diffusion with fast flow paths. Although minor, the difference between pore- and continuum-scale results due to transport controls was discernible with the highly accurate methods employed and is expected to be more significant where heterogeneity is greater, as in natural subsurface materials.

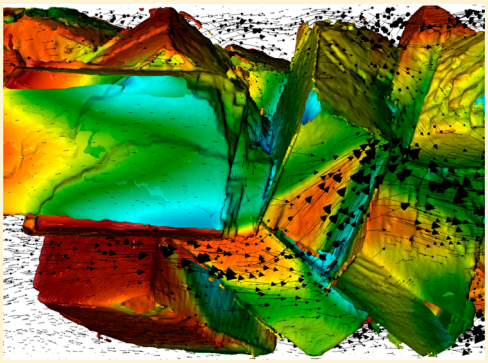

INTRODUCTION

Geologic carbon sequestration (GCS) is considered one of the viable approaches for reducing CO_2 emissions in the atmosphere.[1] Mineral trapping is generally considered to account for a large and most secure portion of the long-term trapping of CO_2 in the subsurface. Trapping involves precipitation of carbonate minerals but in general depends on dissolution of primary minerals as a source of cations as well as alkalinity to raise the solution pH.[2] Prediction of mineral trapping at the reservoir scale thus requires accurate knowledge of mineral precipitation and dissolution rates. Subsurface models used in the prediction of CO_2 sequestration scenarios typically characterize the porous medium as a continuum, where reactive parameters such as reactive surface area and intrinsic reaction rates (mass per unit surface area reactive material) are treated as bulk or averaged properties of the medium. The continuum assumption in the conventional reservoir simulators implies that within each individually resolved spatial element of the model, all solid phases and their reactive surfaces are equally accessible to all fluid phases and that the system is well mixed. However, natural subsurface materials have their own pore-scale (the scale where individual grains and fluid interfaces are resolved) architecture that regulates how physical and chemical processes are coupled. For example, at the pore scale, the hydrologic accessibility of the reactive phases within the pore structure can be effectively resolved.[3,4]

The injection of CO_2 into the subsurface drives the fluid-rock system into "far-from-equilibrium" conditions. The nonlinear dynamics of the reactions coupled to physical processes such as flow and diffusion at the pore scale may result in emergent behavior, including changes in permeability, diffusivity, and reactivity. Dissolution and precipitation can modify the pore structure, potentially increasing the porosity and permeability of the subsurface matrix as well as altering fracture apertures and transmissivity. Rate limitations associated with transport to and from the mineral surface can have an impact on the overall reaction rates. Where these rate limitations operate at the smaller scale (e.g., at the pore scale), they tend not be accounted for in reservoir simulators based on coarse discretization and a continuum-scale assumption. Determination of reaction rates in the laboratory seeks to measure the intrinsic rates of surface reactions free from transport limitations (i.e., the rate of attachment and detachment of ions) using fluidized bed reactors,[5] mixed-flow reactors,[6,7] or rotating disk batch reactors.[6,8,7] However, these limitations are

Received: March 19, 2014
Revised: May 24, 2014
Accepted: May 27, 2014

   dx.doi.org/10.1021/es5013438 | Environ. Sci. Technol. XXXX, XXX, XXX−XXX

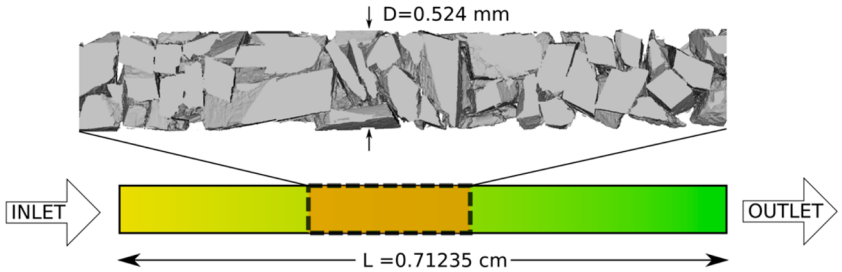

Figure 1. Conceptual 1D model of the capillary (below) and portion of the pore scale domain at 2.32-μm resolution intersected by a plane (above).

potentially important for calcite, which shows a partial diffusion rate control even at 25 °C and circumneutral pH.[6,9]

Research into pore-scale processes has benefitted from recent advances in experimental, imaging and modeling tools. X-ray computed microtomography (XCMT) has been successfully used in a variety of problems related to the pore-scale coupling of structure, hydrogeology, and geochemistry including experiments examining calcite bioprecipitation,[10,11] abiotic calcite precipitation,[9] reactive surface area in geological materials,[4] and multiphase flow in heterogeneous systems.[12] High-performance computing (HPC) tools based on computational fluid dynamics methods have made it possible to simulate reactive transport processes in complex geometries at spatial resolutions in the order of a micrometer.[13] Direct pore-scale models differentiate from other modeling approaches such as pore networks[14] in that they do not need to make any assumption or simplification of the pore space structure. The high spatial resolution makes it possible to capture the interplay between transport processes and surface reaction within the pore space with rigorous description of the physics at the micrometer scale.[2,13,15,16]

In this manuscript, a combination of microscopic characterization, experimental, and modeling approaches are brought to bear on the investigation of the pore-scale controls on calcite dissolution rates under elevated pCO_2 conditions. The objective is to elucidate the relative contributions of transport and surface reactions to effective rates of calcite dissolution in a flow-through capillary tube experiment packed with calcite grains. Effective rates are calculated from effluent concentrations and represent rates that are relevant for application in continuum-scale models. The unprecedented degree of fidelity and accuracy in representing the pore space (imaged by XCMT) as well as the processes of flow and transport in our simulation approach (high-accuracy HPC pore-scale model) makes it possible to identify the most significant sources of uncertainty in representing mineral dissolution kinetics in reactive transport models.

MATERIALS AND METHODS

Laboratory Experiment. Calcite (synthetic Iceland spar) was crushed and sieved to grain sizes between 150 and 250 μm. In a nylon mesh cloth crushed particles were rinsed free of fines with D.I. water, then dried at 50 °C in an oven, and packed into a fused silica capillary tube (665 μm O.D and 535 ± 6 μm I.D, Polymicro Technologies). One end of the capillary was filled with PTFE mesh wires (Mac-Master Carr, 0.015" diameter) to act as a filter plug and to hold the packed calcite particles in place.

A 0.01 M NaCl solution was prepared in a UHP76 stir cell (Advantec MFS, Inc.), equilibrated with 4 bar pCO_2 overnight, and withdrawn into an Isco 65DM pump. Nano tight unions (IDEX Health & Science) were used at both ends of the capillary and connected to 1/32 O.D FEP tubing. An SSI flow-through back pressure regulator (preset at 4 bar pressure) maintained the system pressure, while a 0.5 μm inline filter (IDEX Health & Science) was placed between the packed capillary tube and back pressure regulator.

The pre-equilibrated solution was injected into the packed calcite capillary tube at a constant flow rate of 4.9 ± 0.12 μL/min for 150 min, and the effluent solution was collected every 10 min into a sampling vial. The effluent was analyzed with a PerkinElmer DRC II ICP-MS for calcium concentrations. The crushed calcite capillary tube was flushed clean of residue solution before microtomographic imaging.

Microtomography. The complete assembly was imaged using hard X-ray microtomography at the Advanced Light Source (ALS), Beamline 8.3.2., a flexible facility for characterizing material microstructure on midsized (<1 cm) samples down to submicrometer 3D resolutions. Beamline 8.3.2, which operates on a superconducting bend magnet (11.5 keV critical energy), is described in detail by MacDowell et al.[17] The sample was imaged at 13 keV using a multilayer monochromator and no secondary filters. The detector system was configured with a 35 μm CsI/Be scintillator and a 10× objective to yield a submicrometer voxel size of 899 ± 8 nm. The CCD detector utilized was a PCO-4000 (Cooke Corporation, 4008 × 2672 px). Because of the significant vertical length of the sample in comparison to the field of view, it was scanned as a sequence of 7 "tiled" acquisition runs with a small amount of overlap. Acquisition of each tile required 1801 projections at 1100 ms exposure with interleaved flat field images acquired to correct for temporal variations in beam structure. Raw projections were corrected for dark current and flat field variations, followed by despeckling, ring removal, and filtered back projection reconstruction using the GPU-enabled commercial package Octopus (Inside Matters, formerly inCT).[18] After reconstruction, each of the 7 tiles was 2672 × 1816 × 1816 voxels.

Pore-Scale Domain. A pore-scale simulation domain was constructed from the XCMT images using implicit functions to represent the mineral surface locally on a Cartesian grid. A 2D wavelet transform was used to remove "salt and pepper" noises and to correct uneven illumination regionally in the XCMT images. For segmentation, bi-Gaussian mode identification of the image was used to distinguish between solids, pore space, and artificial "streaks". The resulting discrete, binary (solid or pore) values were used to define a continuous, scalar function by interpolating them between 0.0 and 1.0 over the entire domain. The irregular volumes were defined by intersecting Cartesian cells with a region where the continuous function was less than a threshold equal to 0.5.[19] The simulation domain was represented on a Cartesian grid with a 2.32-μm resolution,

resulting in a domain consisting of 3072 × 256 × 256 grid cells, or approximately 200 million grid points, along with the irregular volume approximations. The technique for constructing the simulation domain is fully consistent with the numerical methods described below.

The length of the pack of crushed calcite grains in the capillary tube was measured from the constructed domain to be 0.71235 cm. To ensure a smooth representation of the inner surface of the capillary tube and differentiate between materials, a numerically generated cylindrical sleeve was superimposed onto the simulation domain. The inner diameter of the capillary tube in the simulations was 524 μm, only slightly smaller than the manufacturer's specifications for the capillary tube (see Figure 1).

Pore-Scale Simulation. Fluid flow in the pore space was modeled with the incompressible Navier–Stokes equations and reactive transport of dissolved components with the advection-diffusion-reaction equation.[13] Flow was solved to steady state before starting the transient reactive transport problem. Geochemical reactions were coupled to transport using the operator splitting approach.[20,21] The governing equations were implemented in the Chombo-Crunch code, which uses an embedded boundary-algebraic multigrid formulation based on a finite volume discretization.[22] Solid–fluid interfaces were represented as embedded boundaries within each of the grid cells.[13] The resulting cut cells were discretized by a finite volume method that accounted for the partial volumes occupied by both fluid and solid and for the interfacial area between fluid and solid. Conservation equations were solved using a predictor-corrector projection method.[23,24] A higher-order upwind method with a van Leer flux limiter was applied to advection terms in a semi-implicit Crank-Nicolson approach to minimize numerical dispersion.[13] Time steps were constrained by the viscous time scale for the flow solution ($5.38 \cdot 10^{-6}$ s) and by the Courant-Friedrichs-Levy criterion for the reactive transport solution ($0.9\ CFL = 2.65 \cdot 10^{-4}$ s). The simulation was carried out using 6,144 processors on *Hopper*, a Cray XE6 system of the National Energy Research Scientific Computing Center (NERSC).

Continuum-Scale Simulation. An equivalent 1-D continuum scale simulation of reactive transport in the capillary tube was performed using the reactive transport code CrunchFlow.[25] The advection-diffusion-dispersion-reaction equations of dissolved components were discretized using an integrated finite difference formulation with 160 grid cells. The third-order time-diminishing variation (TVD) scheme[26] was used for advective transport to minimize numerical dispersion. Geochemical reactions were coupled to transport using an operator splitting approach.[20,21] Simulations were run on a desktop computer (Intel Xeon 3.47 GHz).

Geochemical Simulation. The same geochemical reaction network was used both in the pore-scale and the continuum-scale simulations. Aqueous complexation was modeled as an equilibrium reaction based on a mass action law, while the rate of calcite dissolution was described with a Transition State Theory-based rate law.[27] The system of nonlinear equations was solved using the Newton–Raphson method by the geochemical subroutines in CrunchFlow.[25] Time integration was carried out with a fully implicit, backward Euler step.

RESULTS AND DISCUSSION

Laboratory-Measured Effluent Concentrations. Effluent calcium concentrations measured in the laboratory experiment showed little variation over the 150 min of the experiment (6.06 ± 0.34 mmol L^{-1}), indicating that steady state conditions were reached in a time frame shorter than the 10 min sampling interval (Figure 2a). Mass balance calculations

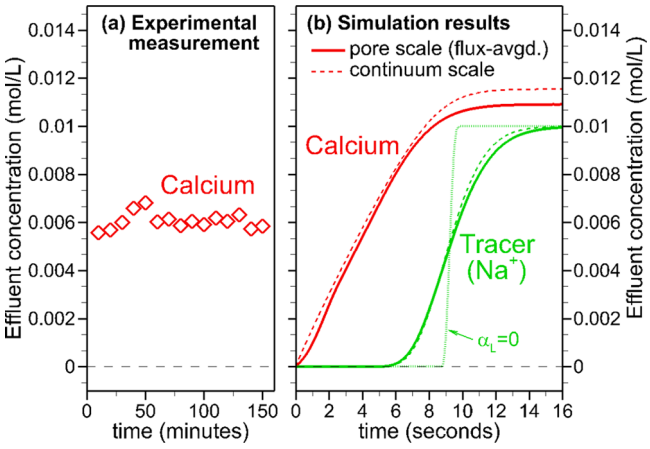

Figure 2. (a) Measured and (b) simulated effluent concentrations for calcium and a nonreactive tracer (sodium). Simulated concentrations consist of flux-averaged pore-scale simulation results and continuum-scale simulation results obtained using a longitudinal dispersivity (α_L) equal to 0.012 cm. Tracer concentrations for a continuum-scale simulation with $\alpha_L = 0$ are also shown for reference. In contrast, the pore-scale simulation does not include any hydrodynamic dispersion, although molecular diffusion is considered.

made assuming that the calcium effluent concentration remained constant over the duration of the experiment indicated that only about 0.02% of the initial calcite dissolved in the 150 min-long experiment. It was thus assumed that the physical changes to the calcite grains brought about by dissolution did not significantly alter porosity or the reactivity of calcite (i.e., surface area and etch pit formation). The small volume of sample collected at each time point (approximately 49 μL) and the difficulty in preventing degassing during collection made it impractical to analyze for dissolved inorganic carbon (DIC) or pH. However, batch calculations using inlet conditions as a starting point indicated that equilibrium concentrations of calcium should be 16.67 mmol L^{-1} (with a DIC of 0.153 mol L^{-1} and a pH of 5.66). Despite the lack of measurements for pH and DIC, the experimentally determined calcium concentration of 6.06 mmol L^{-1}, well below the calculated equilibrium value, strongly suggested that far from equilibrium conditions were maintained in the lab experiment.

Continuum-Scale Simulated Effluent Concentrations. An equivalent 1D continuum model of the capillary was constructed using bulk parameters, which were assumed uniform along the length of the domain. Porosity and surface area parameters were obtained from the pore scale domain, while dispersivity was calibrated using the pore scale simulation results (discussed in the section on Transport Controls below). Porosity was calculated as the sum of the volume occupied by the calcite grains over the volume of the capillary ($\theta = 0.492$), while the bulk surface area was determined as the sum of the interfacial areas of the mineral surfaces over the volume of the capillary ($A_{calcite}$ = 20422 $m^2\ m^{-3}$ bulk = 0.0148 $m^2\ g^{-1}$). This surface area value was close to the value measured by five point krypton BET analysis (0.012 $m^2\ g^{-1}$) on the same Iceland spar in an earlier study.[9] The slightly larger value in this work was

dx.doi.org/10.1021/es5013438 | Environ. Sci. Technol. XXXX, XXX, XXX–XXX

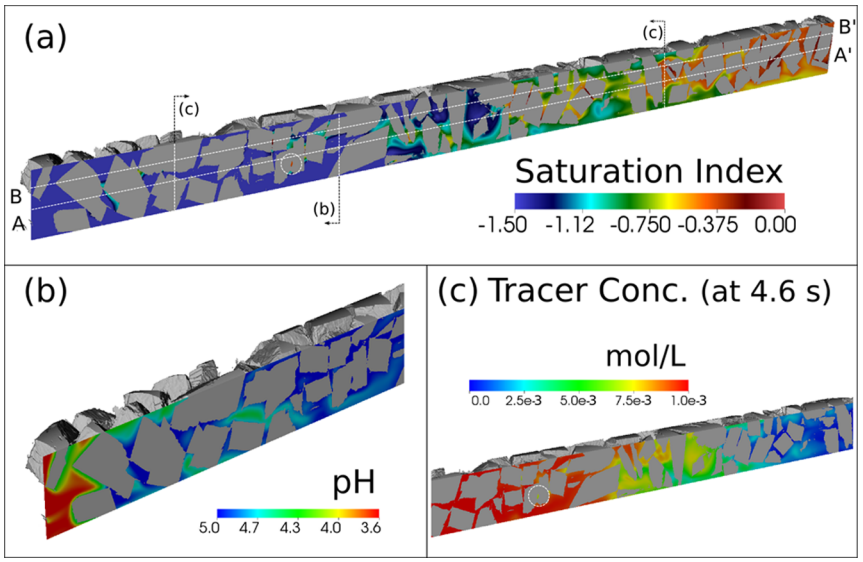

Figure 3. Selected geochemical results from the pore-scale simulation plotted on a plane that intersects the pore-scale domain, with the flow direction being from left to right: (a) Saturation index (log_{10} Q/K_S) contours at 16 s showing the evolution from far-from-equilibrium conditions to near-equilibrium conditions, (b) pH contours at 16 s for the inlet portion the domain showing a significant diffusive boundary layer around the left-most grains, and (c) sodium concentrations in the capillary at 4.6 s, showing the mixing and spreading of the invasion front as well as isolated low-concentration pockets in small pore spaces left behind the front (an example is indicated by a dashed circle).

likely associated with the smaller size of the crushed calcite grains.

Five dissolved components (H^+, H_2CO_3*, Ca^{2+}, Na^+, and Cl^-) and 9 aqueous equilibrium complexation reactions (OH^-, HCO_3^-, CO_3^{2-}, $CaCO_3$(aq), $CaHCO_3^-$, $CaOH^+$, HCl(aq), $CaCl^+$, and $CaCl_2$(aq)) were considered in the simulation. The rate of calcite dissolution was described as the product of a far-from-equilibrium term ($f(a_i)$) and an affinity ($g(\Delta G)$) term that goes to zero at equilibrium

$$r_{CaCO_3} = f(a_i)\cdot g(\Delta G) = (k_1 a_{H^+} + k_2 a_{H_2CO_3*} + k_3)\cdot(1 - 10^{SI}) \quad (1)$$

where k_1, k_2, and k_3 are the rate constants [mol m^{-2} mineral s^{-1}]; a_{H^+} and $a_{H_2CO_3}$* are the activities of H^+ and H_2CO_3* [dimensionless], respectively, and SI is the saturation index (log_{10} Q/K_S) of calcite. In the continuum scale model, the reaction rate calculated by eq 1 in each cell was multiplied by the bulk reactive surface area ($A_{Calcite}$) to obtain the volumetric rate [mol m^{-3} bulk s^{-1}] used in the mass balance equation (see the Supporting Information). The values used for the rate constants are discussed in the section devoted to surface controls on rate.

The steady state effluent concentration of calcium obtained from the continuum-scale model was 11.55 mmol L^{-1}, which compares with an experimentally measured effluent calcium concentration of 6.06 ± 0.34 mmol L^{-1}. Thus, the continuum-scale simulation overestimated the dissolution rates in the laboratory experiment by a factor of 1.9.

Pore-Scale Simulated Effluent Concentrations. A pore-scale simulation was performed to separate the sources of the discrepancy between continuum scale results and experimental results. In contrast to the continuum-scale model, where the reactive surface area was a bulk parameter, calcite dissolution in the pore-scale model was calculated at the calcite grain surfaces. Mass transport of reactants and products in the pore space toward and away from the reactive calcite surfaces was directly solved for (see the Supporting Information). The pore scale simulation was run until steady state conditions were observed in the effluent, which occurred at 16 s. Effluent concentrations from the pore-scale simulation were flux-averaged at the outlet end of the capillary (see the Supporting Information) to obtain a single value that could be compared to experimental and continuum scale simulation results.

The steady state flux-averaged value for the effluent calcium concentration from the pore-scale simulation was 10.91 mmol L^{-1}, slightly lower than the continuum-scale simulated concentration (11.55 mmol L^{-1}). While this difference is small, both of these modeling results were obtained with high-accuracy methods in highly resolved simulation domains. Thus, the difference can be attributed to the different underlying modeling assumptions, implying that transport limitations existed at least locally in the crushed calcite capillary. However, pore-scale simulation results also significantly departed from experimentally measured concentrations, a discrepancy that is explored in the section devoted to surface controls on rates. Insights into the transport limitations are explored on the basis of the highly resolved pore scale results in what follows.

Transport Controls. The solution in the pore space evolved from far-from-equilibrium conditions with respect to calcite near the inlet to near-equilibrium conditions as it flowed around crushed calcite grains in the capillary (Figure 3a). Dissolution of calcite at the grain surfaces caused calcium concentrations and pH to increase, and, in turn, it shifted the carbonate speciation such that although the total carbonate concentration increased, the partial pressure of CO_2 (pCO_2) decreased slightly. Under these conditions, dissolution rates were higher near the inlet (see eq 1). Fluid velocities must go to zero at the mineral surface, resulting in a hydrodynamic boundary layer within which mass transport was dominated by diffusion. Thus, a geochemical gradient drove diffusive transport between the bulk solution and the solution at the grain surface. Under quasi-steady state conditions, diffusive transport of reactants and products was balanced by the

dx.doi.org/10.1021/es5013438 | Environ. Sci. Technol. XXXX, XXX, XXX−XXX

dissolution of calcite at the mineral surface. For the mineral grains near the inlet, reaction rates were sufficiently fast that a large pH gradient was observed in the simulations (Figure 3b). The boundary layers were 55 and 30 μm in width around the first calcite surfaces found along lines A-A′ and B-B′, respectively (see Figure 3a for location). The pH rise across these layer was from 3.8 to 4.5 in A-A′ and from 3.6 to 4.2 in B-B′ (Figure 4a). On the down-gradient side of the same grains, boundary layers were significantly smaller both in terms of pH gradients (5.1 to 5.0 for A-A′ and 4.7 to 4.35 for B-B′) and width, which was reduced to one grid cell (2.32 μm) in both cases. Similarly, boundary layers developed for all variables involved in the calculation of the rate (eq 1) at the mineral surface (pH, CO_2 concentration, calcite saturation index) along the entire length of the capillary domain (Figure 4a-c), although the magnitude of these boundary layers decreased down the length of the capillary in the direction of flow. Within about 2 cm of the inlet, the effect of the boundary layers on the dissolution rate was large and could be attributed solely to the far-from-equilibrium term of the rate expression (Figure 4d), while the near-equilibrium or affinity term played a more significant role in determining the local rate due to transport control as the system moved closer to equilibrium with distance down the capillary tube (Figure 4c). Diffusive boundary layers thus had a stronger effect on rates near the inlet, with calcium concentrations differing significantly from those calculated in the continuum scale model (Figure 5). Due to the tortuous flow paths, mixing increased down stream and the difference between the two models decreased, stabilizing with small fluctuations at about 0.6 mmol L^{-1} (Figure 5).

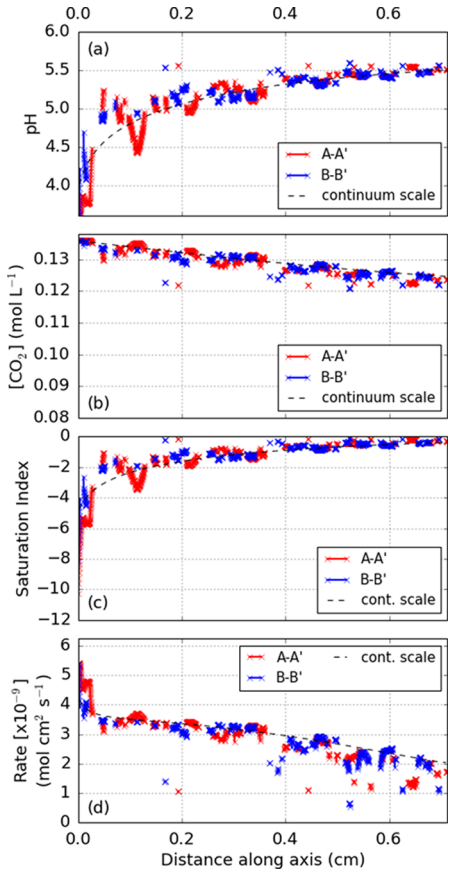

Figure 4. Selected results from the pore-scale simulation are plotted along lines A-A′ and B−B′ (Figure 3a) together with results from the continuum-scale simulation (dashed lines) at time 16 s: (a) pH, (b) CO_2 concentration, (c) saturation index for calcite, and (d) calcite dissolution rate. Gaps in the pore scale data correspond to the location of discrete calcite grains. Pore-scale reaction rates have been calculated from data in plots (a), (b), and (c) according to eq 1, and although they are plotted everywhere in the pore space, they are only applicable at the mineral surface (data point adjacent to the gap) where the reaction is taking place. U-shaped curves (for pH and saturation index) and inverted U-shaped curves (for CO_2 and rates) are the result of transport limitation to rates. Note: Results along lines A-A′ and B−B′ are used to illustrate transport limitations to rates in our domain, but they are only two among ~40,105 different lines that fall within the cylinder at this resolution.

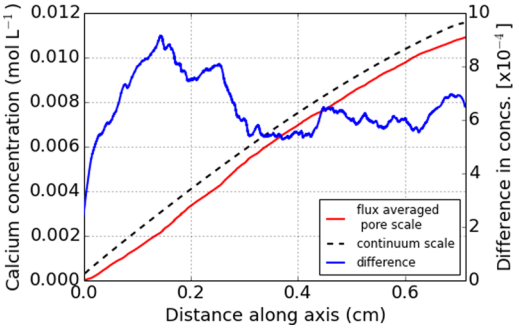

Figure 5. Calcium concentrations along the axis of the cylinder (flow direction) for the continuum-scale simulation compared to flux-averaged values from pore-scale results. Evolution of the difference between the two indicates the discrepancy in rate due to the assumption of well-mixed conditions.

In addition to the outlet end of the capillary, near-equilibrium conditions were also observed in very small pore spaces, despite the fact that far-from-equilibrium conditions dominated in the larger pore spaces (Figure 3a). Near-equilibrium conditions in these small pores indicated that the reaction kinetics were faster than the rate at which reactants were transported into and out of those pore spaces. These spaces were also pores where initial conditions persisted for some time behind the invasion front of sodium, a conservative tracer in the simulation, as it displaced the initial solution (Figure 3c). The slow flushing of the initial conditions from these small pores indicates that they were not in the main flow paths and, thus, fluid velocities there were relatively slow. As a result, transport in and out of these pockets was controlled primarily by diffusion rather than advection. Since the diffusive time scales are larger than those where flow is important, the solution in these small pore spaces was able to equilibrate with calcite.

Further, the geometry of the conservative Na front (Figure 3c) indicated that the variations of velocities within the pore scale resulted in significant mechanical dispersion. The pore scale model results were used to quantify the magnitude of dispersion in the capillary. To do so, continuum-scale simulation results for the effluent concentration of Na were calibrated using dispersivity (α_L) as fitting parameter (Figure 2b). Non-Fickian behavior is observed with pore-scale results showing an early breakthrough and a longer tail (i.e., slower convergence to inlet values). This result agrees with the observation that pore-scale diffusive mass transfer processes between preferential flow paths and relatively immobile zones within primary porosity may have a significant impact on

dx.doi.org/10.1021/es5013438 | Environ. Sci. Technol. XXXX, XXX, XXX−XXX

transport, resulting in long breakthrough tails.[28] The existence of this slower mass transfer resulted in the formation of these pockets under near-equilibrium conditions.

Overall, the assumption of well mixed conditions —the conceptual basis of the continuum scale model— did not apply in the capillary tube because of the local importance of transport limitations to the bulk (or effective) rates. Diffusive boundary layers, particularly near the inlet of the capillary where rates were the highest, contributed to the discrepancy between the pore-scale and the continuum-scale simulation results. Mixing in the complex pore space was significant and contributed to minimize the effect of the diffusive boundary layers on rates. However, pore spaces isolated from the main flow path that exchanged mass with the preferential flow paths by diffusion provided an additional source for discrepancy due to the incomplete mixing.

The effect of transport limitation on rates in this experiment was nevertheless minor, in part because of the aspect ratio of the long and thin capillary tube that behaved almost as a one-dimensional domain. In addition, despite the angular nature of crushed calcite grains, the grains were relatively uniform in size, contributing further to the homogeneity of the porous medium within the capillary. However, the small difference is believed to be accurate; for example, in pore-scale simulations for a capillary tube homogeneously packed with spherical grains,[13] results overlapped perfectly with continuum-scale results. As discussed below, uncertainty in the rate expression and its parametrization accounts for a greater portion of the discrepancy between modeling and experimental results. Nonetheless, one expects these transport limitations associated with diffusion-controlled pore spaces to become more important as heterogeneity increases, whether in the form of pore-scale heterogeneity introduced by a larger range of grain sizes or at larger length scales as a result of a heterogeneous sedimentary fabric.

Surface Controls. The rate constants for calcite dissolution used in the simulations were obtained by fitting the far-from-equilibrium term of eq 1 to the rates reported by Pokrovsky et al.[6,7] in a rotating disk experiment. With this approach, it was assumed that the rates measured by Pokrovsky et al.[6,7] were free of transport limitations. This assumption was justified by the fact that stirring rates used in rotating disk experiments were fast enough to minimize transport limitations. The assumption was required because the pore-scale model calculates the dissolution rate at each mineral surface, where a balance is established between diffusive fluxes and surface rates, accounting for both limitations to rates. Data points used for the fit were limited to those obtained for pCO_2 < 10 atm, a 425-rpm stirring rate, and at 25 °C. Data at 425 rpm were chosen because these experiments covered the range of pH and pCO_2 values in this work; data at faster stirring rates were not considered. The values obtained ($k_1 = 8{\cdot}10^{-6}$, $k_2 = 1.6{\cdot}10^{-8}$, and $k_3 = 1.25{\cdot}10^{-9}$ mol cm^{-2} s) differed from earlier published values;[5,29,30] however, they provided a good fit in order to predict the rates in the range of pH and pCO_2 values in this work (Figure 6).

Additional simulations were performed to calibrate (by trial and error) a single zero-order rate constant (i.e., k_3, with $k_1 = k_2 = 0$ in eq 1) to the effluent calcium concentration measured in the laboratory experiment. For this purpose, the continuum-scale rather than the pore scale model was used due to the large computational costs of the latter. However, in light of the small difference between pore-scale and continuum-scale results

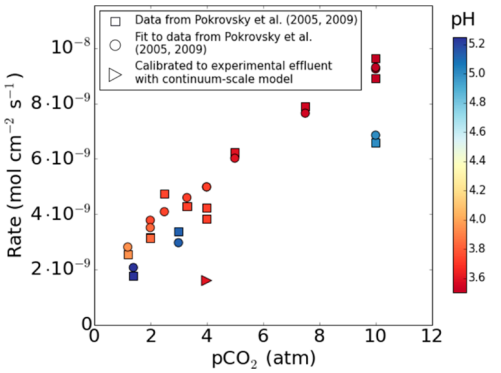

Figure 6. Comparison of calcite dissolution rates. Squares denote data measured by Pokrovsky et al.[6,7] in a rotating disk experiment at 425 rpm. Circles denote the fit employed in this work to the rates reported by Pokrovsky et al.[6,7] using eq 1. The triangle indicates the zero-order rate calibrated from the continuum-scale simulation to the experimentally observed calcium concentration, plotted for the pH and pCO_2 conditions at the inlet as reference.

presented in the previous section, it is assumed that the continuum-scale value is a good estimate for evaluating these purely geochemical effects. The value obtained for k_3 with this method is an evaluation of the surface rate and not an effective rate. The value obtained is plotted in Figure 6 as reference for comparison with the data by Pokrovsky et al.,[6,7] clearly showing that the rate model and the parameter values for the fit overestimated reaction rates in both pore-scale and continuum-scale simulations.

This result was to some extent unexpected for two reasons. First, the rates measured at 425 rpm, the slowest stirring rate employed in Pokrovsky et al.,[6,7] were potentially affected by larger transport limitations than rates at faster stirring rates, which would imply that they could potentially underestimate rates rather than overestimate the rates. The difference between simulated results would have only departed further from measured values if the rate parameters had been calibrated to rates measured to faster stirring rates. Second, as discussed earlier, the reactive surface area estimated geometrically from the calcite grains in the pore scale domain agreed well with BET-measured values on the same material. In order to predict slower reaction rates, lower surface area values would have had to be used (e.g., 45% of the surface area in the continuum-scale model). However, due to the roughness of the surfaces resulting from crushing the calcite grains, one would expect enhanced reactivity, and thus a reactive surface area larger than that evaluated geometrically, not the opposite. The fact that the BET and geometric estimates of the surface area largely agree implies that there is not a great deal of finer nanometer-scale surface roughness.

There are different sources of uncertainty that could explain in part the discrepancy between laboratory measurement and simulated results. The material used in this work was not exactly the same as that used by Pokrovsky et al. (synthetic vs natural Iceland spar obtained from hydrothermal veins in basaltic traps in Central Siberia[6,7]). The pore-scale simulations did not include electrochemical effects in the species diffusion that could have contributed to larger transport limitations and, thus, resulted in lower effective rates. Recently, the applicability of the TST rate formulations has also been called into question on several levels both for dissolution and precipitation. Another issue has to do with the need for multiple rate laws in order to

dx.doi.org/10.1021/es5013438 | Environ. Sci. Technol. XXXX, XXX, XXX–XXX

capture the behavior over the entire range of Gibbs free energies (ΔG). For dissolution, there may be a transition from nearly linear dissolution close to equilibrium to a more nonlinear dependence on ΔG farther from equilibrium as etch pit formation and propagation become more important.[31−33]

Environmental Implications. Whereas the effect of transport limitations on effective rates in this rather (geometrically and chemically) simple experimental setup is minor, the physical and mineralogical heterogeneity of the subsurface environments considered for CO_2 sequestration at different scales (e.g., Landrot et al. 2012[4]) may magnify the impact of this two-way coupling between transport and reactive processes. In particular, trapping of CO_2 in the form of carbonate requires that the pH be increased, generally as a result of the dissolution of cation and alkalinity-bearing phases (e.g., silicates). The pore architecture of natural subsurface materials is complex, and the various phases dissolving and precipitating as well as the CO_2 phase itself need not be strictly colocated. Thus, in some instances there can be a separation in space between the newly formed carbonate and the metal and alkalinity source, particularly under acidic conditions.[34] In this context, transport effects become important in that cations and alkalinity must be moved to the nucleation and growth sites. For example, precipitation of magnesite under high pCO_2 conditions has been experimentally observed to occur in diffusion-dominated microenvironments but not in the main (advection-dominated) paths.[35] Even in the simple pore scale domain studied in the present paper, diffusion-controlled microenvironments were observed (see section on Transport Controls).

Simulations in this work were run to 16 s when steady state conditions (defined by constant effluent concentrations) were reached. These steady state conditions extend further in time (e.g., in the 150 min of the laboratory experiment) but not indefinitely, because dissolution results in pore structure changes. In the dissolution of carbonate minerals under the acidic conditions characterizing CO_2 sequestration, wormholing or "reaction fingering" may occur.[2,36] These emerging processes may magnify the effect of transport limitations in that strongly preferential flow paths can form while diffusion-controlled microenvironments exist between these fast flow paths.

Continuum-scale models for CO_2-induced dissolution in carbonate rocks often require adjustment of the surface area or reaction rate constants to match experimentally measured concentrations even when XCMT information is used to characterize the mineral reactivity (e.g., Hao et al. 2013[36]). While limitations still exist, the approach presented in this work − the combination of a laboratory experiment and a high-resolution pore-scale simulation using image data derived from advanced microscopic characterization techniques− holds promise for providing mechanistic explanations for the understanding and prediction of rates in reactive porous media. The high degree of fidelity in representing the relevant pore-scale processes makes it possible to use the simulations as numerical experiments. This allows for direct quantification of the effects of pore-scale controls on geochemical rates but also for distinguishing these effects from uncertainties in the models of mineral dissolution kinetics. These insights are not available from continuum-scale or pore network models. The experiment presented here yielded minor transport effects on rates. However, it can be argued that the application of the approach to porous media with higher degree of textural and mineralogical heterogeneity can yield to larger differences. High-resolution numerical experiments on experimentally derived image data can be used for deriving upscaled descriptions of geochemical rates applicable to subsurface environments subject to injection of CO_2.

■ ASSOCIATED CONTENT

Ⓢ Supporting Information

Additional text and Tables 1−3. This material is available free of charge via the Internet at http://pubs.acs.org.

■ AUTHOR INFORMATION

Corresponding Author

*Phone: 510-486-7540. E-mail: smolins@lbl.gov. Mail Stop: 74R316C.

Notes

The authors declare no competing financial interest.

■ ACKNOWLEDGMENTS

This material is based upon work supported as part of the Center for Nanoscale Control of Geologic CO_2, an Energy Frontier Research Center funded by the U.S. Department of Energy, Office of Science, Office of Basic Energy Sciences, and the Office of Advanced Scientific Computing Research (D.T., T.L., and C.S.), under contract number DE-AC02-05CH11231. This research also used resources of the National Energy Research Scientific Computing Center, supported by the U.S. DOE Office of Science (DE-AC02-05CH11231). XCMT imaging was performed with the assistance of Alastair MacDowell and Dula Parkinson at the Advanced Light Source, Beamline 8.3.2, supported by the U.S. DOE Office of Science, Office of Basic Energy Sciences (DE-AC02-05CH11231). The work presented in this manuscript has greatly benefitted from discussion of the results with members of the Center.

■ REFERENCES

(1) Pacala, S.; Socolow, R. Stabilization Wedges: Solving the Climate Problem for the Next 50 Years with Current Technologies. *Science* **2004**, *305* (5686), 968.

(2) Steefel, C. I.; Molins, S.; Trebotich, D. Pore Scale Processes Associated with Subsurface CO_2 Injection and Sequestration. *Rev. Mineral. Geochem.* **2013**, *77*, 259−303.

(3) Peters, C. A. Accessibilities of reactive minerals in consolidated sedimentary rock: An imaging study of three sandstones. *Chem. Geol.* **2009**, *265* (1−2), 198−208.

(4) Landrot, G.; Ajo-Franklin, J. B.; Yang, L.; Cabrini, S.; Steefel, C. I. Measurement of accessible reactive surface area in a sandstone, with application to CO_2 mineralization. *Chem. Geol.* **2012**, *318−319* (0), 113−125.

(5) Chou, L.; Garrels, R.; Wollast, R. Comparative-study of the kinetics and mechanisms of dissolution of carbonate minerals. *Chem. Geol.* **1989**, *78* (3−4), 269−282.

(6) Pokrovsky, O. S.; Golubev, S. V.; Schott, J. Dissolution kinetics of calcite, dolomite and magnesite at 25 °C and 0 to 50 atm pCO_2. *Chem. Geol.* **2005**, *217* (3−4), 239−255.

(7) Pokrovsky, O. S.; Golubev, S. V.; Schott, J.; Castillo, A. Calcite, dolomite and magnesite dissolution kinetics in aqueous solutions at acid to circumneutral pH, 25 to 150 °C and 1 to 55 atm pCO_2: New constraints on CO_2 sequestration in sedimentary basins. *Chem. Geol.* **2009**, *265* (1−2), 20−32.

(8) Schott, J.; Brantley, S.; Crerar, D.; Guy, C.; Borcsik, M.; Willaime, C. Dissolution kinetics of strained calcite. *Geochim. Cosmochim. Acta* **1989**, *53* (2), 373−382.

(9) Noiriel, C.; Steefel, C. I.; Yang, L.; Ajo-Franklin, J. Upscaling calcium carbonate precipitation rates from pore to continuum scale. *Chem. Geol.* **2012**, *318*−*319* (0), 60−74.
(10) Wu, Y.; Ajo-Franklin, J.; Spycher, N.; Hubbard, S.; Zhang, G.; Williams, K.; Taylor, J.; Fujita, Y.; Smith, R. Geophysical monitoring and reactive transport modeling of ureolytically-driven calcium carbonate precipitation. *Geochem. Trans.* **2011**, *12* (1), 7.
(11) Armstrong, R.; Ajo-Franklin, J. Investigating biomineralization using synchrotron based X-ray computed microtomography. *Geophys. Res. Lett.* **2011**, DOI: DOI: 10.1029/2011GL046916.
(12) Kneafsey, T. J.; Silin, D.; Ajo-Franklin, J. B. Supercritical CO_2 flow through a layered silica sand/calcite sand system: Experiment and modified maximal inscribed spheres analysis. *Int. J. Greenhouse Gas Control* **2013**, *14* (0), 141−150.
(13) Molins, S.; Trebotich, D.; Steefel, C. I.; Shen, C. An investigation of the effect of pore scale flow on average geochemical reaction rates using direct numerical simulation. *Water Resour. Res.* **2012**, DOI: DOI: 10.1029/2011WR011404.
(14) Nogues, J. P.; Fitts, J. P.; Celia, M. A.; Peters, C. A. Permeability evolution due to dissolution and precipitation of carbonates using reactive transport modeling in pore networks. *Water Resour. Res.* **2013**, *49* (9), 6006−6021.
(15) Yoon, H.; Valocchi, A. J.; Werth, C. J.; Dewers, T. Pore-scale simulation of mixing-induced calcium carbonate precipitation and dissolution in a microfluidic pore network. *Water Resour. Res.* **2012**, DOI: doi:10.1029/2011WR011192.
(16) Hiorth, A.; Jettestuen, E.; Cathles, L.; Madland, M. Precipitation, dissolution, and ion exchange processes coupled with a lattice Boltzmann advection diffusion solver. *Geochim. Cosmochim. Acta* **2013**, *104*, 99−110.
(17) MacDowell, A. A.; Parkinson, D. Y.; Haboub, A.; Schaible, E.; Nasiatka, J. R.; Yee, C. A.; Jameson, J. R.; Ajo-Franklin, J. B.; Brodersen, C. R.; McElrone, A. J. X-ray micro-tomography at the Advanced Light Source. *Proc. SPIE* **2012**, *8506*, 850618−850618−14.
(18) Vlassenbroeck, J.; Masschaele, B.; Cnudde, V.; Dierick, M.; Pieters, K.; Van Hoorebeke, L.; Jacobs, P. *Advances in X-ray Tomography for Geomaterials*; Chap. Octopus 8: A High Performance Tomographic Reconstruction Package for X-ray Tube and Synchrotron micro-CT, ISTE: 2010; pp 167−173.
(19) Ligocki, T. J.; Schwartz, P. O.; Percelay, J.; Colella, P. Embedded boundary grid generation using the divergence theorem, implicit functions, and constructive solid geometry. *J. Phys. Conf. Ser.* **2008**, *125* (1), 1−5.
(20) Yeh, G. T.; Tripathi, V. S. A critical evaluation of recent developments in hydrogeochemical transport models of reactive multichemical components. *Water Resour. Res.* **1989**, *25* (1), 93−108.
(21) Steefel, C.; MacQuarrie, K. Approaches to modeling of reactive transport in porous media. *Rev. Mineral. Geochem.* **1996**, *34*, 83−129.
(22) Trebotich, D.; Adams, M. F.; Molins, S.; Steefel, C. I.; Shen, C. High resolution simulation of pore scale reactive transport processes associated with carbon sequestration. *Comput. Sci. Engin.* 2014, accepted.
(23) Trebotich, D. P.; Colella, P. A Projection Method for Incompressible Viscous Flow on Moving Quadrilateral Grids. *J. Comput. Phys.* **2001**, *166* (2), 191−217.
(24) Colella, P.; Graves, D. T.; Keen, B.; Modiano, D. A Cartesian Grid Embedded Boundary Method for Hyperbolic Conservation Laws. *J. Comput. Phys.* **2006**, *211* (1), 347−366.
(25) Steefel, C. I.; Carroll, S.; Zhao, P.; Roberts, S. Cesium migration in Hanford sediment: a multisite cation exchange model based on laboratory transport experiments. *J. Contam. Hydrol.* **2003**, *67* (1−4), 219−246.
(26) Gupta, A.; Lake, L.; Pope, G.; Sepehrnoori, K.; King, M. High-resolution monotonic schemes for reservoir fluid-flow simulation. *In Situ* **1991**, *15* (3), 289−317.
(27) Lasaga, A. C. Transition state theory. *Rev. Mineral. Geochem.* **1981**, *8* (1), 135−168.
(28) Scheibe, T. D.; Hou, Z.; Palmer, B. J.; Tartakovsky, A. M. Pore-Scale simulation of intragranular diffusion: Effects of incomplete mixing on macroscopic manifestations. *Water Resour. Res.* **2013**, *49*, 1−18.
(29) Plummer, L.; Wigley, T.; Parkhurst, D. Kinetics of calcite dissolution in CO_2-Water systems at 5 °C to 60 °C and 0.0 to 1.0 atm CO_2. *Am. J. Sci.* **1978**, *278* (2), 179−216.
(30) Palandri, J.; Kharaka, Y. A compilation of rate parameters of water-mineral interaction kinetics for application to geochemical modeling; Open File Report 2004−1068; U.S. Geological Survey: 2004.
(31) Burch, T.; Nagy, K.; Lasaga, A. Free energy dependence of albite dissolution kinetics at 80°C and pH 8.8. *Chem. Geol.* **1993**, *105* (1−3), 137−162.
(32) White, A. F.; Brantley, S. L. The effect of time on the weathering of silicate minerals: why do weathering rates differ in the laboratory and field? *Chem. Geol.* **2003**, *202* (3 - 4), 479−506.
(33) Maher, K.; Steefel, C. I.; White, A. F.; Stonestrom, D. A. The role of reaction affinity and secondary minerals in regulating chemical weathering rates at the Santa Cruz Soil Chronosequence, California. *Geochim. Cosmochim. Acta* **2009**, *73* (10), 2804−2831.
(34) Daval, D.; Martinez, I.; Corvisier, J.; Findling, N.; Goffé, B.; Guyot, F. Carbonation of Ca-bearing silicates, the case of wollastonite: Experimental investigations and kinetic modeling. *Chem. Geol.* **2009**, *265* (1 - 2), 63−78.
(35) Yang, L.; Steefel, C. I.; Bechtel, H. Microfluidic and Capillary Tube Experimental Study of Forsterite Carbonation by CO_2 Bearing Fluids. In *Abstract V41A-2773 presented at 2013 Fall Meeting*, AGU: San Francisco, CA, Dec 3−7, 2013.
(36) Hao, Y.; Smith, M.; Sholokhova, Y.; Carroll, S. CO_2-induced dissolution of low permeability carbonates. Part II: Numerical modeling of experiments. *Adv. Water Resour.* **2013**, *62* (0), 388−408.